

High-resolution study of outflow activity and chemical environment of Chamaeleon-MMS1

VERONICA ALLEN,^{1,2,3} MARTIN A. CORDINER,^{4,5} GILLES ADANDE,^{3,4} STEVEN B. CHARNLEY,⁴ YI-JEHNG KUAN,^{6,7} AND
EVA WIRSTRÖM⁸

¹*Kapteyn Astronomical Institute, University of Groningen
9747 AD Groningen, the Netherlands*

²*NWO Veni Fellow*

³*NASA Postdoctoral Program fellow*

⁴*NASA Goddard Space Flight Center
8800 Greenbelt Road
Greenbelt, MD 20771, USA*

⁵*Institute for Astrophysics and Computational Sciences, The Catholic University of America
Washington, DC 20064, USA*

⁶*Department of Earth Sciences, National Taiwan Normal University
Taipei, 11677, Taiwan, ROC*

⁷*Institute of Astronomy and Astrophysics, Academia Sinica
Taipei, 10617, Taiwan, ROC*

⁸*Department of Space, Earth, and Environment, Chalmers University of Technology
Onsala Space Observatory
439 92 Onsala, Sweden*

(Received 2023)

Submitted to ApJ

ABSTRACT

The earliest stages of low-mass star-formation are unclear, but it has been proposed that Chamaeleon-MMS1 is a candidate First Hydrostatic Core (FHSC), the transition stage between a prestellar and protostellar core. This work describes the local (~ 4000 AU) outflow activity associated with Chamaeleon-MMS1 and its effect on the surrounding material in order to determine the evolutionary state of this young low-mass source. We used the Atacama Large Millimeter/sub-millimeter Array (ALMA) to observe Chamaeleon-MMS1 at 220 GHz at high spatial (~ 75 AU) and spectral resolutions ($0.1\text{--}0.3$ km s⁻¹). A low energy outflow is detected through its interaction with the surrounding cloud. The outflow consists of two components, a broad spectral feature ($\Delta v \sim 8$ km s⁻¹) to the northeast and narrow spectral features ($\Delta v \sim 1$ km s⁻¹) to both the northeast and southwest. The molecular tracers CS, formaldehyde (H₂CO), and methanol (CH₃OH) were used to analyze the effect of the outflow on the surrounding gas as well as determine the rotational temperature of this gas. The rotational temperature of H₂CO is calculated to be 40 K toward the continuum source with similarly low temperatures (10–75 K) toward clumps affected by the outflow. CH₃OH is only detected toward gas clumps located away from the continuum source, where the methanol is expected to have been released by the energy of the outflow through ice sputtering in shock waves. Chamaeleon-MMS1 shows outflow activity with the power source likely being a single precessing outflow. While molecular emission and high outflow speeds rule it out as a FHSC, the outflow is less energetic than outflows detected from other Class 0 objects. The inferred gas temperatures toward the continuum source are also relatively low, indicating that Cha-MMS1 is one of the youngest known sources.

Keywords: Interstellar Medium: Young Stellar Objects — Star Formation — individual objects: Cha-MMS1 — stellar winds

1. INTRODUCTION

Understanding star formation is a central problem in astrophysics, with direct implications for our understanding of how galaxies evolve and how planets and life form. Stars form in collapsing cores, corresponding to the densest regions within molecular clouds, but the precise details of this process are still far from being completely understood, particularly during the initial collapse period. The numerical hydrodynamic simulations of [Larson \(1969\)](#), more recently by [Masunaga & Inutsuka \(2000\)](#), [Machida et al. \(2008\)](#), and [Tomida et al. \(2010\)](#), show that the collapse of a molecular cloud is arrested by thermal pressure once the density (n) becomes sufficiently great that cooling by dust radiation is inhibited (at $n \gtrsim 10^{11} \text{ cm}^{-3}$). At this point, a quasi-hydrostatic object is formed, known as the First Hydrostatic Core (FHSC). The FHSC is calculated to persist in an approximately adiabatic state for $\sim 10^3$ yr, which is a sufficiently short time to make it a rare object in nearby star-forming regions. Observational signatures of the FHSC include a low luminosity ($\sim 0.01\text{--}0.1 L_{\odot}$), and an approximately thermal spectral energy distribution that peaks in the far-infrared/sub-mm range ([Saigo & Tomisaka 2011](#)). A low luminosity source is generally considered to be a FHSC candidate if it shows little to no emission at wavelengths $< 70 \mu\text{m}$. Calculations show that the FHSC should also produce a slow molecular outflow, which extends up to a distance of a few hundred AU from the core ([Machida et al. 2008](#); [Tomida et al. 2010](#)). Typically, slow uncollimated outflows are expected, but [Price et al. \(2012\)](#) demonstrated that collimated jets with velocities up to 7 km s^{-1} are possible during the FHSC phase.

Several FHSC candidates are currently identified. These include L1451-mm ([Pineda et al. 2011](#)); NGC 1333 - IRAS 4C ([Koumpia et al. 2016](#)); L1535-NE/MC35-mm ([Fujishiro et al. 2020](#)); Oph A N6 and Oph A SM1 ([Friesen et al. 2018](#)); and G208.89-20. ([Dutta et al. 2022](#)); and perhaps Per-Bolo 45 [Maureira et al. \(2020\)](#). Distinguishing between an FHSC and a very low luminosity Class 0 protostar (known as a VeLLO) has proven difficult, in part due to a lack of detailed spectro-spatial information on outflow properties. VeLLOs appear to be young, low-mass protostars undergoing episodic accretion, and a number of these were identified by the c2d Spitzer survey of [Dunham et al. \(2008\)](#). The list of very low luminosity protostars includes IRAS 15398-3359 ([Okoda et al. 2020](#)); L673-7 IRS ([Dunham et al. 2011](#)); L1014 IRS ([Dunham et al. 2011](#)); L1148 IRS ([Dunham et al. 2011](#)); GSS30, SM1N, B2-A7 and IRAS 16267-2417 in Oph A ([Friesen et al. 2018](#)), as well as sources formerly iden-

tified as FHSC candidates: B1b-N ([Marcelino et al. 2018](#)) and B1b-S ([Hirano 2019](#)); Per-Bolo 58, L1448 IRS 2E and L1448 IRS 2E ([Maureira et al. 2020](#)); CB17-MMS ([Spear et al. 2021](#)). The physics, chemistry, and observational signatures of FHSCs and VeLLOs have been discussed by [Omukai \(2007\)](#), [Lee \(2007\)](#), and [Young et al. \(2019\)](#). Specifically, CS emission was modeled to exist only in the central few AU around a late-stage FHSC.

Chamaeleon-MMS1 (Cha-MMS1) is a young protostar located at a distance of 192 pc ([Dzib et al. 2018](#)) with a systemic velocity of 4.5 km s^{-1} ([Belloche et al. 2006](#)) and was first detected in 1.3 mm emission by [Reipurth et al. \(1996\)](#). The central object is deeply embedded inside a dense molecular cloud ([Cordiner et al. 2012](#)) and has been classified by [Belloche et al. \(2006, 2011\)](#) as either an extremely young VeLLO or an FHSC with an internal luminosity between 0.08 and $0.18 L_{\odot}$ ([Tsitali et al. 2013](#)). [Belloche et al. \(2006\)](#) did not find any evidence of CO outflow activity from Cha-MMS1 using single-dish (APEX) observations, and the studies by [Hiramatsu et al. \(2007\)](#); [Ladd et al. \(2011\)](#) determined that the nearby HH 49/50 outflow is driven by the more evolved Class I protostar Ced 110 IRS 4. [Ladd et al. \(2011\)](#) determined from single-dish CO observations that the IRS 4 outflow is deflected around (or grazes the edge of) the $100''$ -diameter dense clump that contains the collapsing protostar Cha-MMS1. [Väisälä et al. \(2014\)](#) analyzed NH_3 and continuum emission toward Cha-MMS1 using the Australia Telescope Compact Array (ATCA) and concluded that a warm central source was within, but it was at the Class 0 stage at the latest. Recently, [Busch et al. \(2020\)](#) published an analysis of the CO(3-2) emission tracing outflow activity associated with Cha-MMS1. The outflow in that article is qualitatively similar to the CO(2-1) emission in this work, but we also present the outflow activity as traced by CS, H_2CO , and CH_3OH , showing different structures than those traced by the CO observation. Additionally, analysis of multiple FHSC candidates (including Cha-MMS1) using dense envelope tracers was published by [Maureira et al. \(2020\)](#). Both studies conclude that Cha-MMS1 is at a very young evolutionary state.

In this paper, we present the high-angular resolution analysis of the outflow activity associated with Cha-MMS1 and their effect on the surrounding material. In §2, we give details of the ALMA observations and data reduction. §3 contains the details of five detected species including isotopologs (CO, ^{13}CO , CS, H_2CO and CH_3OH), analysis of the outflow mechanical properties, and determination of the rotational temperature of various sub-regions in this source. §4, we

discuss the implications of our results, and in §5 we present our conclusions regarding the nature of this extremely young protostellar object.

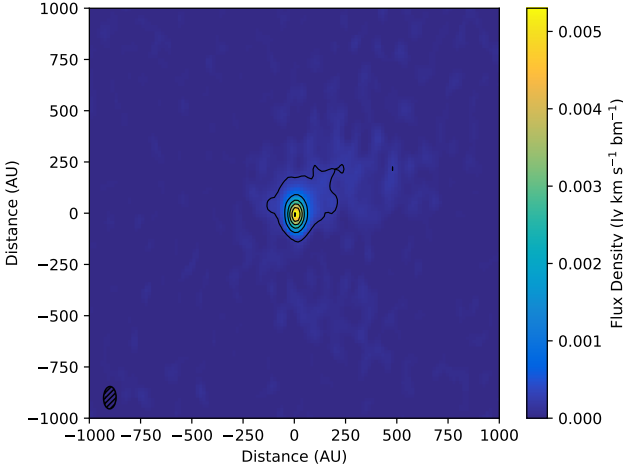


Figure 1. 220 GHz continuum map of Cha-MMS1. Contours start at 3σ (with an rms of 0.21 mJy/beam) continue at 1.05, 2.10, 3.15, 4.20, and 5.25 mJy/beam with a peak of 6.48 mJy/beam. The beam size is $0.72'' \times 0.41''$.

Table 1. Targeted spectral lines (E_{up} and A_{ij} from CDMS)

Species	Transition	Frequency (GHz)	E_{up} (K)	$\log(A_{ij})$
CO	2-1	230.5380	16.6	-6.16
^{13}CO	2-1	220.3986	15.9	-6.22
CS	5-4	244.9355	35.3	-3.53
H_2CO	$3_{0,3}-2_{2,1}$	218.2221	20.9	-3.55
H_2CO	$3_{2,2}-2_{2,1}$	218.4756	68.1	-3.80
H_2CO	$3_{1,2}-2_{1,1}$	225.6977	33.4	-3.56
CH_3OH	$5_{3,2}-4_{3,1}$	218.4400	45.5	-4.33
CH_3OH	$5_{-1,5}-4_{-1,4}$	241.7672	40.4	-4.24
CH_3OH	$5_{0,5}-4_{0,4}++$	241.7914	34.8	-4.22
HC_3N	24-23	218.3247	131.0	-3.08

2. OBSERVATIONS AND DATA REDUCTION

Cha-MMS1 was observed using the Atacama Large Millimeter/sub-millimeter Array (ALMA) on 16 July 2014 and 6 and 7 June 2015 using 26 antennas on 16 July, and 37-39 antennas on 6 and 7 June (project code 2013.1.01113.S) with an angular resolution of $\sim 0.7''$ and spectral resolutions of $\sim 0.08 \text{ km s}^{-1}$ in three spectral windows (covering ^{12}CO , ^{13}CO and CS), 0.17 km s^{-1} for H_2CO (218222 MHz), and 0.3 km s^{-1} in the other four spectral windows. The calibrators used were Callisto, Ganymede, J0635-7516, J1058-8003, J1208-7809, J1107-4449, and J0538-4405. The pointing position of our ALMA observations was the millimeter

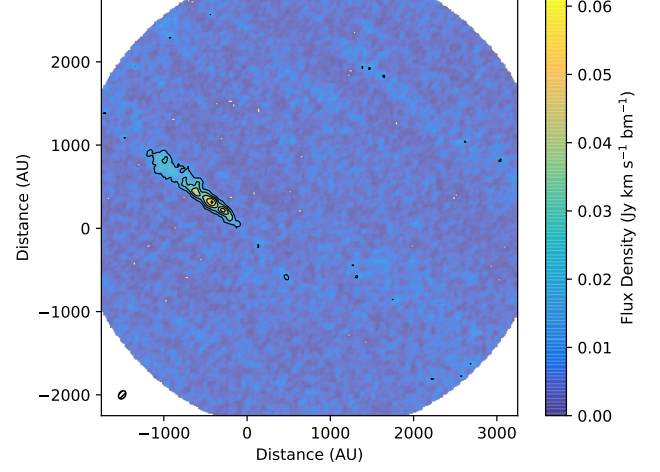


Figure 2. Primary beam corrected integrated intensity map (between 8.7 and 17.1 km s^{-1}) of broad component of CO outflow. Contours start at 3σ (rms of 12 mJy/beam km s^{-1}) continue in intervals of 3σ to a peak of 61 mJy/beam km s^{-1} . The beam size is $0.72'' \times 0.52''$.

position reported in Reipurth et al. (1996) rather than the Spitzer IR peak, therefore the source is consistently offset in our maps. Data reduction was performed with the CASA package (version 5.4.0). Corresponding spectral windows from different observation dates were concatenated and the continuum was subtracted. Imaging was done using the tclean process with a Hogbom deconvolver and Briggs weighting with a robust parameter of 0.5 and all images are primary beam corrected. The RMS noise for line-free channels was typically 2-4 mJy.

3. RESULTS

3.1. Continuum and Line Detection

Figure 1 shows the compact, unresolved continuum emission at 220 GHz detected toward Cha-MMS 1. Our observations targeted several molecular species expected in very young low-mass star-forming regions summarized in Table 1. ^{12}CO emission is resolved out on large scales, but a weak spectral feature covering the broad velocity range of 8.7 - 17.1 km s^{-1} is detected in ^{12}CO to the northeast of the continuum source (§ 3.2.1, Figure 2). Moment maps were also made of narrow spectral features in ^{12}CO and ^{13}CO (§ 3.2.2, Figures 3 and 4). There is self-absorption in both ^{12}CO and ^{13}CO with no signal for each in the ranges 4.0 - 5.7 km s^{-1} and 4.4 - 5.1 km s^{-1} , respectively. ^{13}CO shows strong emission towards the continuum source and weak emission (less than 3σ) cospatial with the narrow red ^{12}CO emission southwest of the continuum source. CS emission is clumpy and, on larger spatial scales, the CS clumps seem to trace out a cone (§ 3.3, Figure 6). Within $1.5''$ (288 AU) of the continuum source spectral emission of CS shows an hourglass-

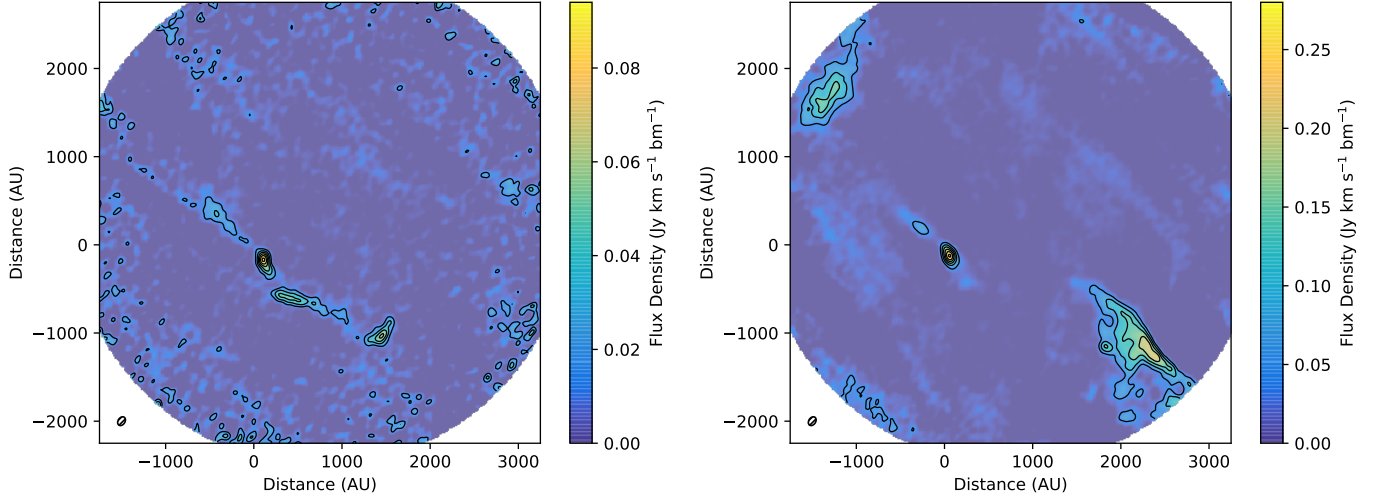


Figure 3. Primary beam corrected integrated intensity maps for ^{12}CO narrow emission features. The continuum peak is located at 0,0 AU. The beam size is $0.72'' \times 0.52''$. (left) Integrated intensity map (between 5.7 and 8.7 km s^{-1}) of narrow red-shifted component of CO outflow. Contours start at 3σ (rms of 15 mJy/beam km s^{-1}) continue in intervals of 3σ to a peak of 94 mJy/beam km s^{-1} . (right) Integrated intensity map (between 1.8 and 4.0 km s^{-1}) of narrow blue-shifted lobes of CO outflow. Contours start at 3σ (rms of 45 mJy/beam km s^{-1}) continue in intervals of 3σ up to a peak of 277 mJy/beam km s^{-1} .

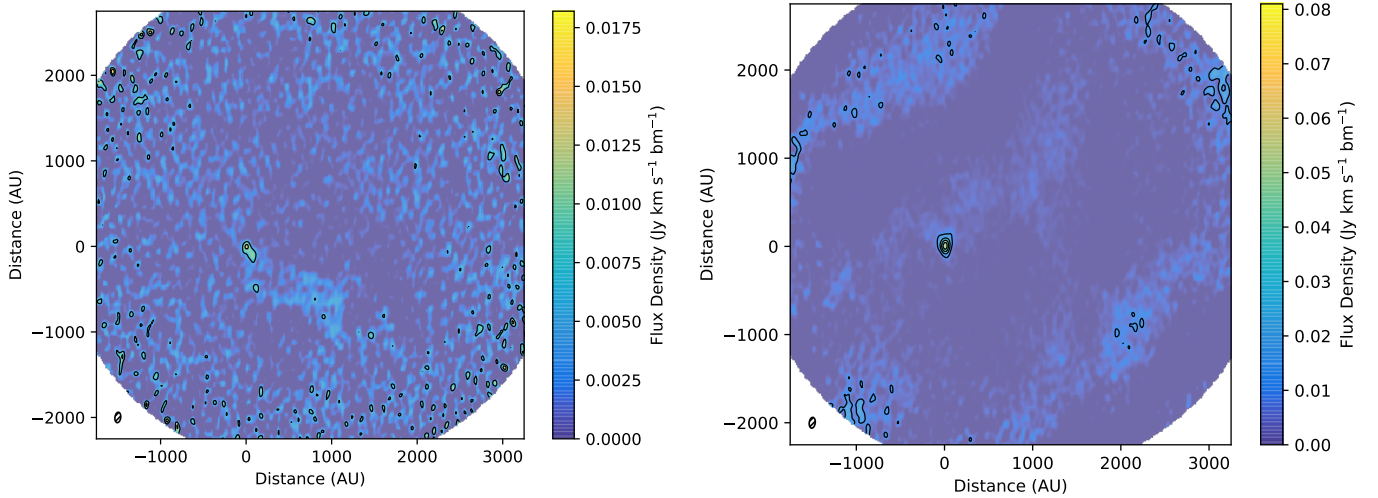


Figure 4. Primary beam corrected integrated intensity maps for ^{13}CO emission features. The continuum peak is located at 0,0 AU. The beam size is $0.82'' \times 0.45''$ (left) Integrated intensity map (between 5.1 and 6.0 km s^{-1}) of red component of ^{13}CO outflow. Contours start at 3σ (rms of 3.1 mJy/beam km s^{-1}) continue in intervals of 1σ to a peak of 18.1 mJy/beam km s^{-1} . (right) Integrated intensity map (between 3.5 and 4.4 km s^{-1}) of blue component of ^{13}CO outflow. Contours start at 3σ (rms of 12 mJy/beam km s^{-1}) continue in intervals of 3σ to a peak of 80.6 mJy/beam km s^{-1} .

like morphology. Three H_2CO lines were detected (§ 3.4, Figure 15) showing emission in different regions, most of which correspond with the locations of CS emission. Three weak CH_3OH transitions were detected at 5- to 10σ RMS levels (§ 3.5) coinciding with the H_2CO emission that is not coincident with the Cha-MMS1 core. The targeted HC_3N transition was not detected.

3.2. Outflow activity

The emission detected in ^{12}CO was used to determine the properties of outflow activity associated with this source. Both the red and blue lobes of the narrow outflow component are located toward the northeast and southwest of the continuum source with an additional broad red component appearing to the northeast.

3.2.1. Broad red outflow component

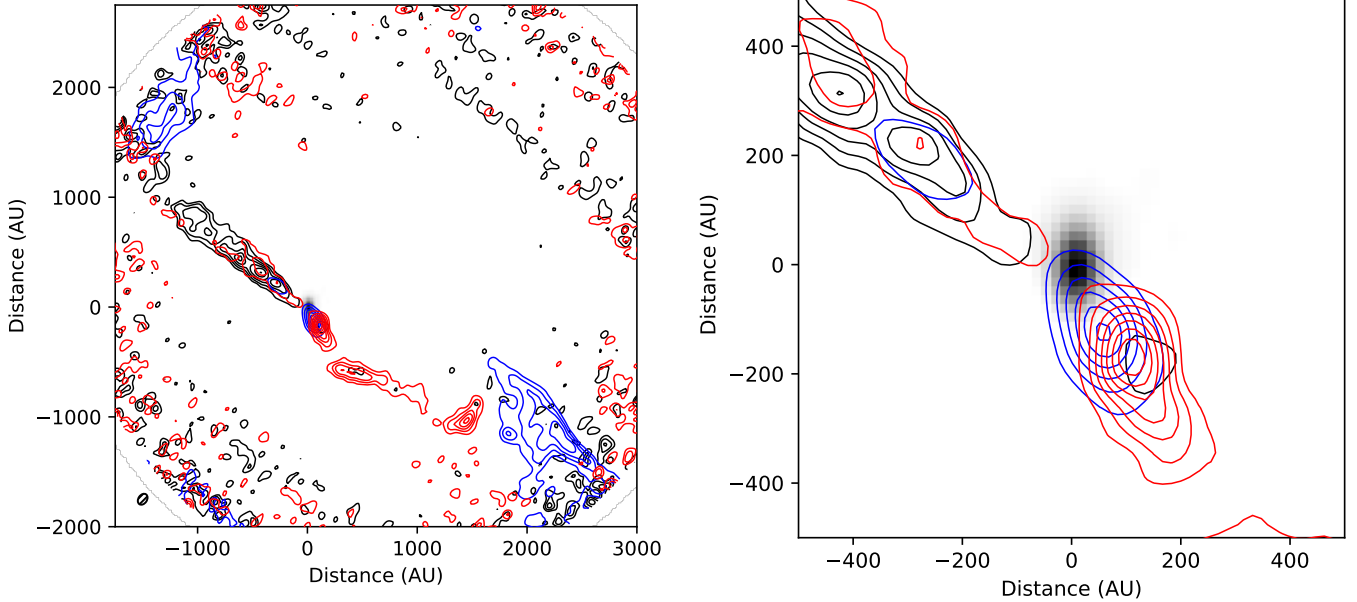


Figure 5. Primary beam corrected integrated intensity image of the ^{12}CO emission over the red-shifted, narrow velocity range from 5.7 to 8.7 km s^{-1} (red contours) and the blue-shifted, narrow velocity range from 3.5 to 4.4 km s^{-1} (blue contours). The ^{12}CO emission of the red-shifted, broad velocity range from 8.7 to 17.1 km s^{-1} is shown in black contours and all are overlaid on the continuum emission of Cha-MMS1 (greyscale). Contours are as in Figures 2 and 3. The *left* figure shows the full extent of the emission and the *right* figure shows the detail of the inner 1000 AU. The beam size is $0.72'' \times 0.52''$.

A weak, broad red-shifted outflow is detected to the northeast of the continuum source in ^{12}CO (Figure 2). It is quite collimated with a collimation factor of 5.5. A Gaussian fit made to this component of the ^{12}CO emission shows that the center is at $10.9 \pm 0.2 \text{ km s}^{-1}$ and the full-width half-maximum (FWHM) is $6.7 \pm 0.4 \text{ km s}^{-1}$. The blue counterpart to the southwest is not nearly as broad or collimated (see Figure 3 right). A Gaussian fit of the southern blue component has a central velocity of $3.40 \pm 0.01 \text{ km s}^{-1}$ and a FWHM of $0.77 \pm 0.03 \text{ km s}^{-1}$. This much narrower spectral line may not be the opposite component of the broad red outflow, but no broader blue component was detected. No broad component is detected in ^{13}CO (Figure 4).

3.2.2. Narrow bipolar outflow

The left frames of Figures 3 and 4 show ^{12}CO and ^{13}CO integrated intensity maps (between 5.7 and 8.7 km s^{-1} and 5.1 and 6.0 km s^{-1} , respectively) of spectrally narrow red-shifted outflow activity to the south of the continuum source which coincide in an 'S'-like shape. The blue components of ^{12}CO (Figure 3 right) are both to the northeast and southwest at the edges of the field-of-view. These blue components appear to be the ends of the outflow, but as we do not have a larger field-of-view, we cannot confirm. The line profiles of the ^{12}CO components are narrow at $1.4 \pm 0.1 \text{ km s}^{-1}$ (southern red) and $0.72 \pm 0.07 \text{ km s}^{-1}$ (northern blue) with central peaks near v_{LSR} of Cha-MMS1 at $6.94 \pm 0.04 \text{ km s}^{-1}$ and $3.55 \pm 0.03 \text{ km s}^{-1}$. The spectral lines for ^{13}CO are even

narrower at 0.34 ± 0.02 and 0.35 ± 0.01 with central peaks at 5.47 ± 0.01 and 3.565 ± 0.006 for the red and blue lobes, respectively. All three components of the ^{12}CO outflow – broad red, narrow red, and narrow blue – are shown in Figure 5. Details of the spectra across the region can be found in Appendix A in Figures 11 and 12.

3.2.3. Mechanical outflow properties

We used the approach described in Sánchez-Monge et al. (2013) and López-Sepulcre et al. (2009) to calculate the mechanical outflow properties. The measured properties for each outflow lobe are: the difference between the maximum velocity and systemic velocity (v_{max}), the length of the major axis (at the 5σ contour), the area of the outflow (as an ellipse), and the integrated intensity of the emission between v_{max} and 2σ from the line peak ($\int T_{\text{mb}} dv$). The CO column density was determined assuming optically thin emission as in Goldsmith & Langer (1999) equations (10) and (19) assuming excitation temperatures of 10, 20, and 30 K. The calculated CO column densities varied by a factor of 3–4 between the different temperatures, so we used the average for calculating the hydrogen column density (N_{H_2}) assuming a CO abundance of 10^{-4} , as is typical (Bolatto et al. 2013). Because the CO emission showed strong self-absorption at velocities near the velocity of the system ($v_{\text{LSR}} = 4.9 \text{ km s}^{-1}$), the CO intensities were corrected assuming an τ value of 5.

The other calculated properties are: outflow mass (calculated using the area of the outflow lobe and the mass of the

Table 2. Calculated mechanical outflow properties from CO emission (errors in parentheses) assuming $\tau=5$. V_{\max} is the observed maximum velocity wrt V_{LSR} . Velocity dependent properties are calculated assuming an inclination of 80° . V_{dep} is the deprojected maximum velocity taking into account the outflow direction. Derived value ranged based on the trends in [Wu et al. \(2004\)](#) for a young star with a L_{bol} of 0.08-0.18 are started in the column "Calculated" with non-derivable velocity-based properties marked with †.

	Northern Red	Southern Red	Northern Blue	Southern Blue	Calculated
V_{\max} (km s $^{-1}$)	12.4 (0.1)	4.0 (0.1)	3.2 (0.1)	2.9 (0.1)	†
V_{dep} (km s $^{-1}$)	71.8 (0.6)	23.4 (0.6)	18.6 (0.6)	16.8 (0.6)	†
t_{kin} (yr)	130 (10)	490 (20)	720 (20)	800 (30)	†
Outflow mass (M_\odot)	$5.2 (1.0) \times 10^{-5}$	$7.4 (1.7) \times 10^{-5}$	$4.7 (0.6) \times 10^{-5}$	$2.1 (0.1) \times 10^{-4}$	$2.2\text{-}3.5 \times 10^{-2}$
Mass-loss rate (M_\odot yr $^{-1}$)	$4.1 (1.2) \times 10^{-7}$	$1.5 (0.4) \times 10^{-7}$	$3.3 (0.7) \times 10^{-7}$	$3.1 (0.3) \times 10^{-7}$	†
Momentum (M_\odot km s $^{-1}$)	$3.7 (0.8) \times 10^{-3}$	$1.7 (0.4) \times 10^{-3}$	$9.9 (1.2) \times 10^{-4}$	$9.4 (0.7) \times 10^{-3}$	†
Kinetic Energy (erg)	$2.6 (0.5) \times 10^{42}$	$4.0 (0.9) \times 10^{41}$	$1.6 (1.9) \times 10^{41}$	$5.9 (0.4) \times 10^{41}$	†
Mechanical Luminosity (L_\odot)	$1.1 (2.7) \times 10^{-1}$	$5.7 (3.1) \times 10^{-3}$	$2.3 (0.8) \times 10^{-3}$	$2.4 (0.2) \times 10^{-2}$	$2.2\text{-}3.6 \times 10^{-3}$
Momentum rate (M_\odot km s $^{-1}$ yr $^{-1}$)	$2.9 (0.7) \times 10^{-5}$	$3.6 (1.4) \times 10^{-6}$	$1.4 (0.1) \times 10^{-6}$	$1.1 (0.1) \times 10^{-5}$	$2.2\text{-}4.0 \times 10^{-6}$

hydrogen from the calculated H_2 column density), the dynamical or kinetic time – t_{kin} (the length of the outflow lobe divided by v_{\max}), kinetic energy (outflow mass times $0.5 v_{\max}^2$), momentum (outflow mass times v_{\max}), momentum rate – which is also called the force (momentum/ t_{dyn}), mass-loss rate (outflow mass/ t_{dyn}), and mechanical luminosity (kinetic energy/ t_{dyn}). As the direction of the outflow is near the plane of the sky, we applied the inclination correction factors from [López-Sepulcre et al. \(2010\)](#) assuming an inclination of 80° . We determined this inclination geometrically taking into account the opening angle of the northern red outflow and the presence of red and blue components in each direction.

The mechanical outflow properties are summarized in Table 2 for the detected outflow lobes. The fast broad outflow component (northern red) has a maximum relative velocity of ~ 12 km s $^{-1}$ (deprojected to ~ 70 km s $^{-1}$). The narrow components have a maximum velocity of ~ 4 km s $^{-1}$ (deprojected to ~ 20 km s $^{-1}$). Using the trends outlined in [Wu et al. \(2004\)](#), we calculated the momentum rate, outflow mass, and mechanical luminosity expected from a young star with a L_{bol} of 0.08-0.18. The momentum rate would be $2.2\text{-}4.0 \times 10^{-6} M_\odot$ km s $^{-1}$ yr $^{-1}$, the outflow mass $2.2\text{-}3.5 \times 10^{-2} M_\odot$, and the mechanical luminosity $2.2\text{-}3.6 \times 10^{-3} L_\odot$. The outflows described in this paper have a mass 100-1000 times lower, and a momentum rate and mechanical luminosity comparable to the calculated value.

3.3. CS

Figure 6 shows CS emission tracing a wide cone on larger scales, indicating the interaction between multiple outflows and the surroundings or a steep precessing angle of a single outflow. Alternatively, this morphology could be due to a spatially wider and low-velocity component tracing the cavity walls, as is commonly found towards other protostellar outflows. On smaller scales, the CS emission is hourglass-shaped and the first moment (velocity) maps (Figure 7) show

inverse velocity gradients immediately above and below the continuum source.

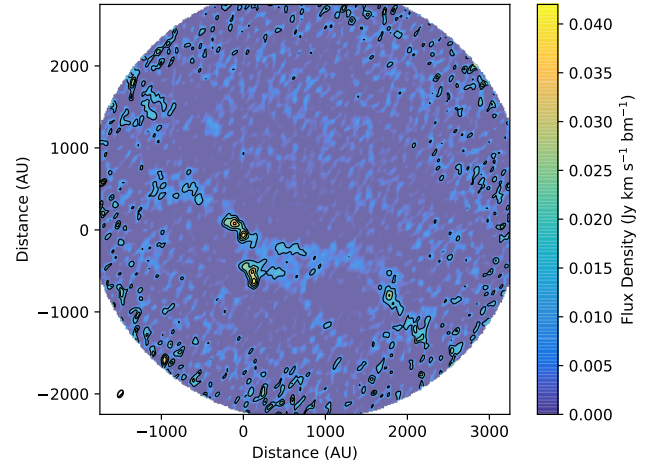


Figure 6. Primary beam corrected integrated intensity map (between 3.7 and 5.5 km s $^{-1}$) of CS emission. Contours start at 3σ (rms of 9 mJy/beam km s $^{-1}$) continue in intervals of 3σ to a peak of 42.2 mJy/beam km s $^{-1}$. The beam size is $0.65'' \times 0.39''$.

3.4. H_2CO emission

H_2CO emission is detected toward the continuum as well as about $3''$ (~ 600 au) to the south of the continuum source, about $16''$ (3100 au) southwest of the continuum source, and $7.5''$ (1500 au) northeast of the continuum source in all three detected transitions. We labeled these regions Main, south (S), west (W), and north (N) (See Figure 8). The emission from H_2CO in these three regions coincides with CS emission in all cases, but does not show the hourglass morphology toward the central source (Main) seen in CS. Cha-MMS1 W corresponds to the southwestern lobe of the CO outflow emission. There is emission detected from the H_2CO transition at 218.222 GHz about $10a''$ (1900 au) north-northeast

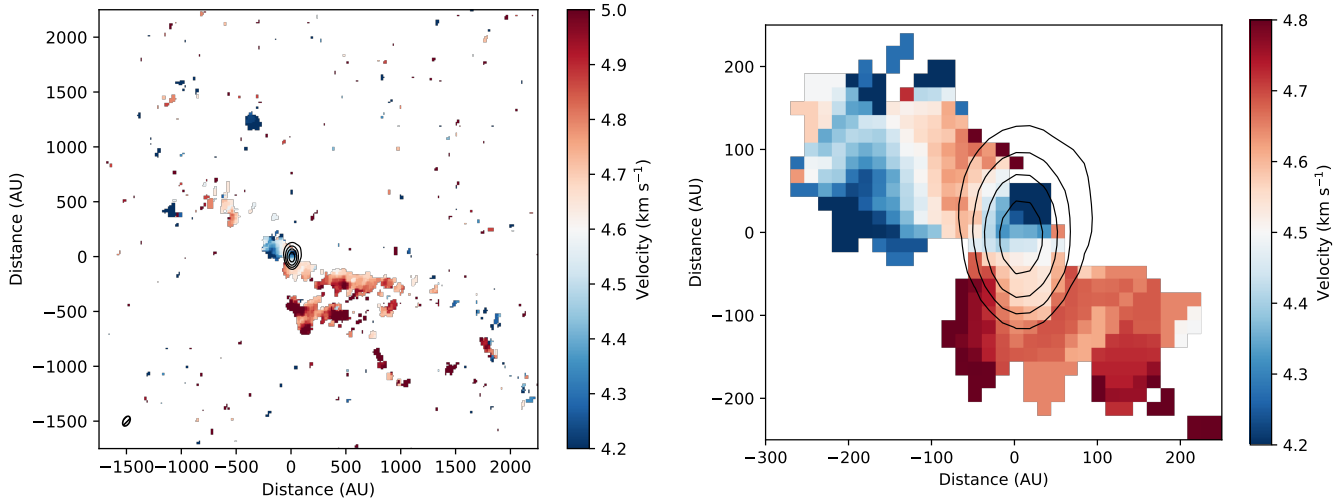


Figure 7. Colored pixels correspond to the velocity at each point. The black contours show the continuum source. **Left:** First moment map (velocity) of CS emission across the field-of-view. **Right:** As in Left, but focused on emission near the continuum source.

of the continuum source, but the emission detected in this area from the other two transitions is very weak. The higher energy H_2CO transition at 218.475 GHz ($E_{\text{up}}=68$ K) shows very weak emission in each region (see Appendix A for spectra).

Table 3 shows the rotational temperatures and column densities determined using the H_2CO transitions in a rotational diagram in the CASSIS software¹ and the CDMS database. Rotational temperatures range from ~ 25 K to 51 K with a temperature of $51.0 (\pm 36.2)$ K toward the continuum source. The column densities are consistently $\sim 10^{13} \text{ cm}^{-2}$. The gas in these condensations appears to be sufficiently dense for the rotational temperature, gas temperature, and dust temperature to be equal ($n > 10^{4.5} \text{ cm}^{-3}$ from Goldsmith (2001)). In this case, based on the experimentally-measured sublimation temperature (144 K, Noble et al. (2012)), it is unlikely that the detected H_2CO originates in thermal desorption from warm dust. A gas-phase origin in reactions between oxygen atoms and CH_3 radicals is possible.

Table 3. H_2CO gas properties in different regions of Cha-MMS1 with errors in parentheses. Note that the fit for N was poor due to the low flux of the transition at 219475 MHz ($E_{\text{up}} 68$ K).

Region	T_{rot} (K)	N_{col} (cm^{-2})
Main	40.4 (+2.7, -2.4)	$3.8 (0.4) \times 10^{13}$
N	73 (+101, -27)	$2.8 (+0.08, -0.01) \times 10^{13}$
S	10.8 (+0.3, -0.2)	$1.4 (0.1) \times 10^{13}$
W	36.5 (+7.0, -5.1)	$3.9 (+1.2, -0.9) \times 10^{13}$

¹ <http://cassis.irap.omp.eu> (Vastel et al. 2015). CASSIS has been developed by IRAP-UPS/CNRS.

3.5. CH_3OH emission

CH_3OH emission is detected towards the clumps associated with H_2CO emission to the northeast, south, and southwest of the continuum source, but not toward the continuum source itself. All CH_3OH emission is much weaker than in other detected species. The column densities are consistent between regions at 10^{13} - 10^{14} cm^{-2} (Table 4). The upper limit for the column density of CH_3OH toward the main source was calculated assuming a T_{rot} of 51 K (to match the temperature of H_2CO toward Main) and a line width of 0.7 km s^{-1} . The inferred dust temperatures are significantly lower than the sublimation temperature of CH_3OH derived from experiments (128 K; Pentead et al. (2017)) and so the

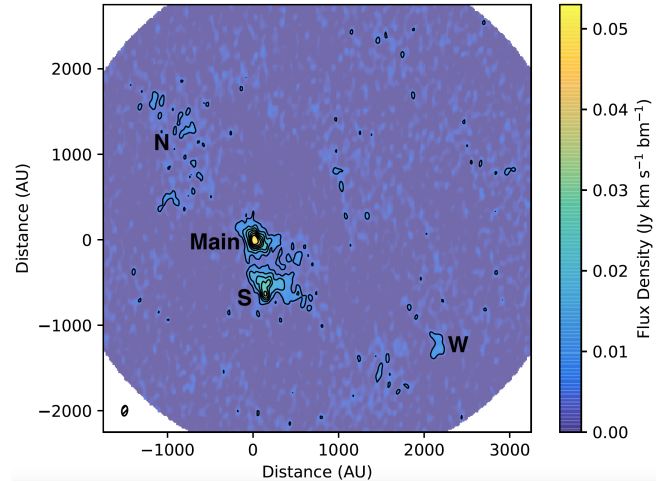


Figure 8. Primary beam corrected integrated intensity map (between 3.1 and 5.5 km s^{-1}) for H_2CO transitions at 218.222 GHz. The continuum peak is at $0,0$ au. Contours start at 3σ (rms of $6 \text{ mJy/beam km s}^{-1}$) continue in intervals of 3σ to a peak of $53 \text{ mJy/beam km s}^{-1}$. The beam size is $0.80'' \times 0.43''$.

observed methanol is likely being produced by ice sputtering in shock waves.

Table 4. CH₃OH gas properties in different regions of Cha-MMS1. * The rotational temperature of CH₃OH towards Main was assumed to be 51 K to mirror H₂CO toward Main and the column density is therefore an upper limit.

Region	T_{rot} (K)	N_{col} (cm ⁻²)
Main	51*	$<1.2 \times 10^{13}$
N	41.2 (30.8)	$8.6 (6.4) \times 10^{13}$
S	23.2 (2.3)	$4.8 (0.8) \times 10^{13}$
W	15.7 (1.9)	$1.1 (0.4) \times 10^{14}$

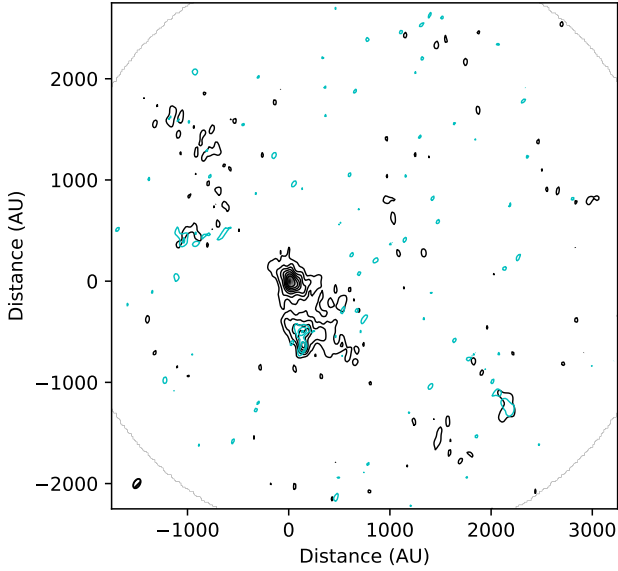


Figure 9. Primary beam corrected integrated intensity maps for H₂CO (218.222 GHz) and CH₃OH (241.791 GHz). Black contours show H₂CO as in Figure 8. Cyan CH₃OH contours (integrated between 3.6 and 5.4 km s⁻¹) start at 3 σ (rms of 6.6 mJy/beam km s⁻¹) and continue in 1 σ intervals to a peak of 25 mJy/beam km s⁻¹. The continuum is shown in greyscale coincident with H₂CO emission, but not CH₃OH.

4. DISCUSSION

4.1. Physical origin of outflow emission

The CO emission has multiple spatially overlapping components indicating that the outflow is nearly perpendicular to the line-of-sight. The shape of the red-shifted emission in CO and ¹³CO to the southwest of the continuum source implies that there is a dense clump of molecular gas diverting the outflowing material, which is traced in our observations by H₂CO and CH₃OH. This is also suggested in [Maureira](#)

[et al. \(2020\)](#) in maps of NH₂D. The alternative scenario is that this S-shaped emission and slower, more distant blue-shifted emission indicates a precessing outflow. The broad red-shifted emission to the northeast of the continuum may originate from a second source implying a tight binary system within the continuum. There is no corresponding blue-shifted broad component detected at similar velocities but it may have been disrupted by the molecular clump south of the continuum source. The irregular velocity structure demonstrates that in the early stages of star formation, the outflow launching is chaotic. The clumpy structure observed in CS and H₂CO emission may be due to small ejections from the early stages of the stellar outflow or simply the clumpiness of the surrounding cloud. The underlying power source driving the outflow activity associated with Cha-MMS1 could be either a single precessing outflow or two outflows from a close binary system. Alternative scenarios can also produce outflow precession, for instance, the misalignment between the outflow axis (a proxy for angular momentum axis) and the magnetic field axis as discussed in [Busch et al. \(2020\)](#), which does not require a binary. Similarly, a change in the angular momentum axis of the infalling material due to turbulent conditions can also produce shape distortions ([Matsumoto et al. 2017](#)).

4.2. Status of Cha-MMS1

While many FHSC candidates have been proposed over the past 20 years, most have now been identified as young class 0 objects, VeLLOs, or prestellar cores. Compared to the outflow properties of the remaining FHSC candidates with published outflow properties (G208.89-20.04 [Dutta et al. \(2022\)](#), MC35-mm (I1535-NE) [Fujishiro et al. \(2020\)](#), L1451-mm [Pineda et al. \(2011\)](#), and GF 9-2 [Furuya et al. \(2019\)](#)) Cha-MMS1 has a similar maximum velocity range, generally lower dynamical time, and higher mechanical luminosity (by at least 2 orders of magnitude). The mechanical luminosity is also several orders of magnitude higher than the VeLLOs identified in [Dunham et al. \(2011\)](#). The sources with the most similar outflow properties are the young stars in Barnard 1b ([Hirano & Liu 2014](#)). Numerous complex molecular lines have been detected toward B1b-S ([Marcelino et al. 2018](#)), indicating that it is too evolved to be a FHSC.

4.2.1. Mechanical properties

The mechanical outflow properties are several orders of magnitude lower than a 1 L_☉ star. The mechanical properties we have derived for Cha-MMS1 are in line with the relationships between mass and luminosity and momentum rate and luminosity shown in [Wu et al. \(2004\)](#). The line of sight outflow properties we calculated using the CO (2-1) transition are generally similar to the values in [Busch et al. \(2020\)](#), which were calculated using the CO (3-2) transition. They concluded that Cha-MMS1 was not a FHSC, though it was

one of the youngest Class 0 objects ever detected. We find the kinetic time to be on the order of hundreds of years, rather than thousands, which results in our time-dependent values being an order of magnitude higher. We agree with their assessment that the bent shape of the red-shifted emission in CO and ^{13}CO to the southwest of the continuum source is likely due to the clump of molecular material there.

4.2.2. Chemistry

The presence of H_2CO without corresponding CH_3OH towards the main source is striking and attests to the young age of this source. CH_3OH is also underabundant with respect to the $\text{CH}_3\text{OH}/\text{H}_2\text{CO}$ ratio typically observed in the vicinity of low and high-mass protostars (van der Tak et al. 2000). Using detected emission from three H_2CO transitions and three CH_3OH , we created rotational diagrams to determine the gas temperature and column density at the four positions described in the previous section: main, N, S and W. The resulting gas temperatures at Cha-MMS1 main and W are ~ 50 K, indicating dust temperatures below those required to thermally desorb H_2CO (114 K) from icy dust grain mantles. The low dust temperature inferred from the temperature of CH_3OH is too cool for thermal desorption, which implies that this emission arises from ice sputtering from interactions with the out-flowing material, as CH_3OH is not easily made in the gas phase. The rotational temperatures for the emission at Cha-MMS1 S suggest dust temperatures lower than the sublimation temperature of both H_2CO and CH_3OH , therefore may also be the result of outflow shocks sputtering ices.

5. CONCLUSIONS

We observed Cha-MMS1 with ALMA in Band 6 at high angular resolution and detected ^{12}CO and ^{13}CO emission as well as CS, H_2CO , and CH_3OH . We find a weak outflow nearly perpendicular to the line of sight toward the northeast and southwest of the continuum source. The effects of the outflow are seen on the local molecular cloud through CS, H_2CO , and CH_3OH emission. A kink in the southwestern outflow corresponds with low rotational temperature (~ 20 – 30 K) emission from H_2CO and CH_3OH indicating a clump of molecular material being shocked by the outflow.

Comparison of Cha-MMS1 with other low-luminosity protostars supports the view that it is not a viable FHSC. In fact, recent observations of SiO and CH_3OH in L1451-mm (Wakelam et al. 2022) suggest that it too is not a FHSC. The weak outflow and relatively low temperatures associated with this object indicate that it is one of the youngest known Class 0 objects.

Acknowledgments: This paper makes use of the following ALMA data: ADS/JAO.ALMA 2013.1.01113.S. ALMA is a partnership of ESO (representing its member states), NSF

(USA), and NINS (Japan), together with NRC (Canada) and NSC and ASIAA (Taiwan), in cooperation with the Republic of Chile. The Joint ALMA Observatory is operated by ESO, AUI/NRAO, and NAOJ. The National Radio Astronomy Observatory is a facility of the National Science Foundation operated under a cooperative agreement by Associated Universities, Inc. V. Allen’s research for this article was supported by an appointment to the NASA Postdoctoral Program at the NASA Goddard Space Flight Center, administered by Universities Space Research Association under contract with NASA. V. Allen is currently supported by an NWO Veni grant number VI.Veni.202.135. V. Allen, M. Cordiner, and S.B. Charnley were supported by the NASA Planetary Science Division Internal Scientist Funding Program through the Fundamental Laboratory Research work package (FLaRe).

Facilities: ALMA

APPENDIX

A. SPECTRA

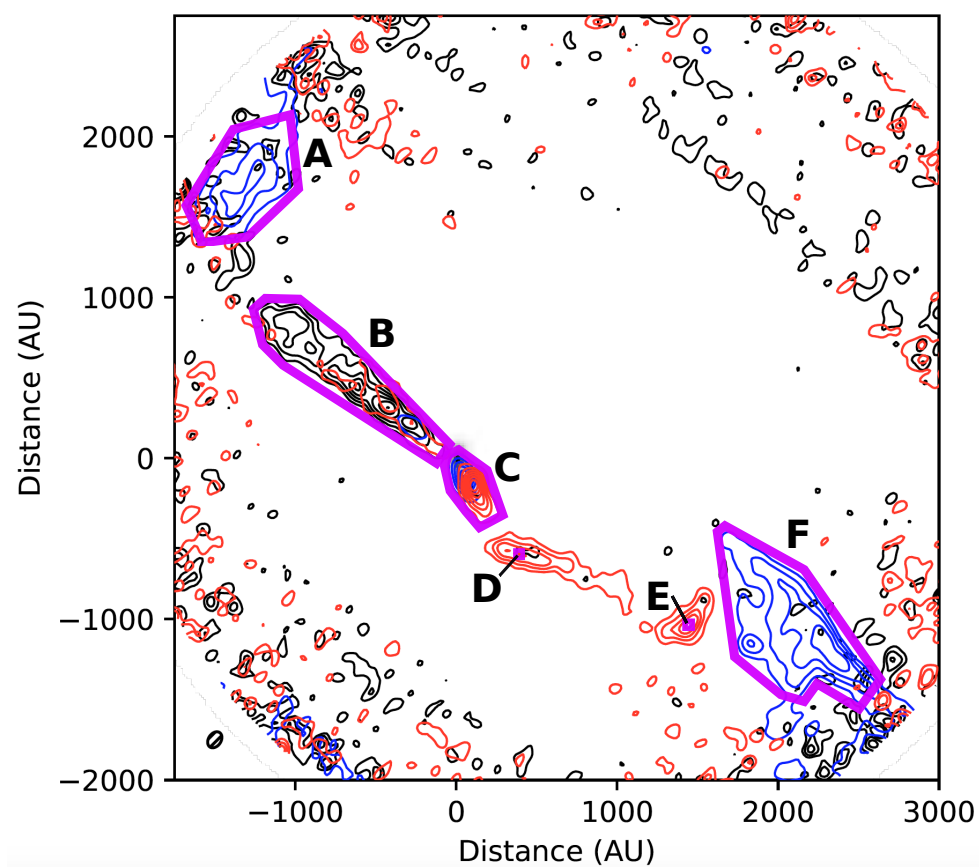


Figure 10. Integrated intensity maps of CO as in Figure 5 with sub-regions labeled A-F. All spectra are integrated over the area surrounded in magenta, except D and E which are taken from the emission peak.

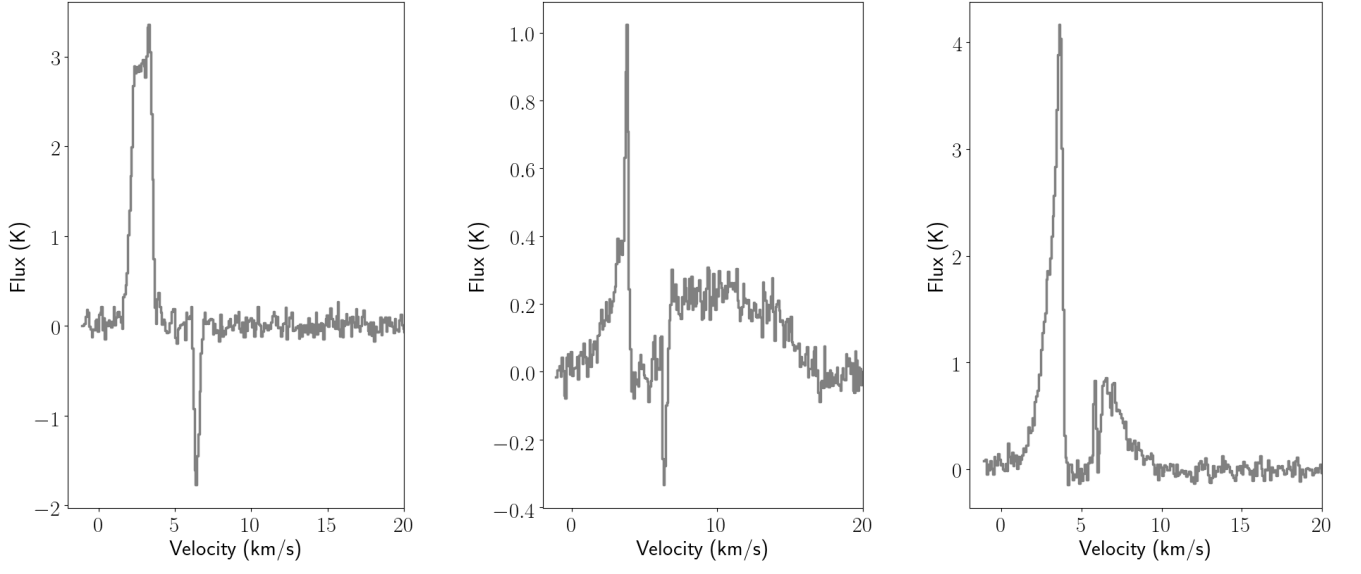


Figure 11. CO spectra toward sub-regions A, B, and C (*left to right*) from Figure 10.

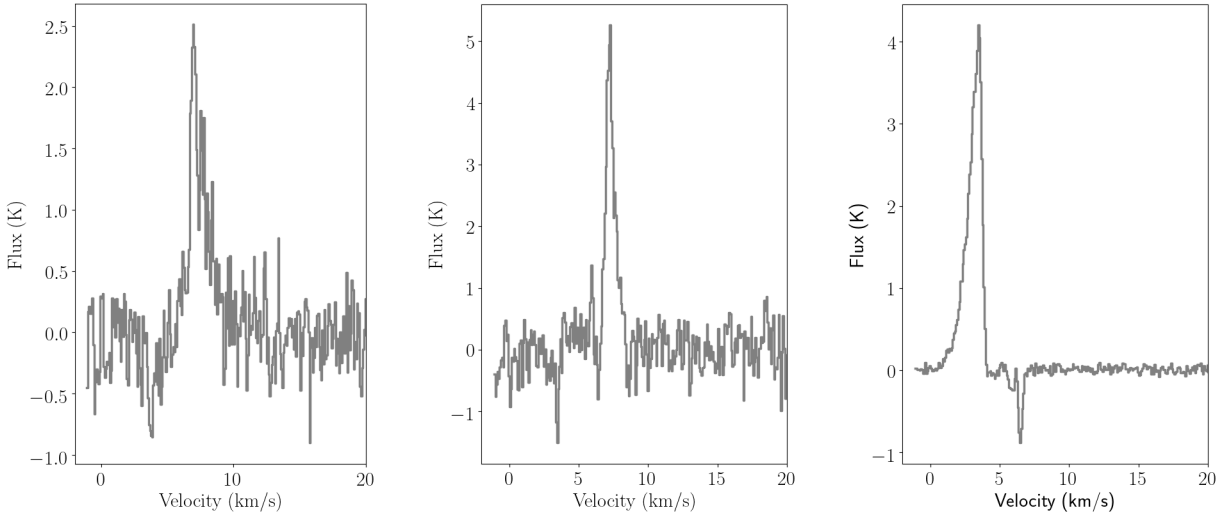


Figure 12. CO spectra toward sub-regions D, E, and F (*left to right*) from Figure 10.

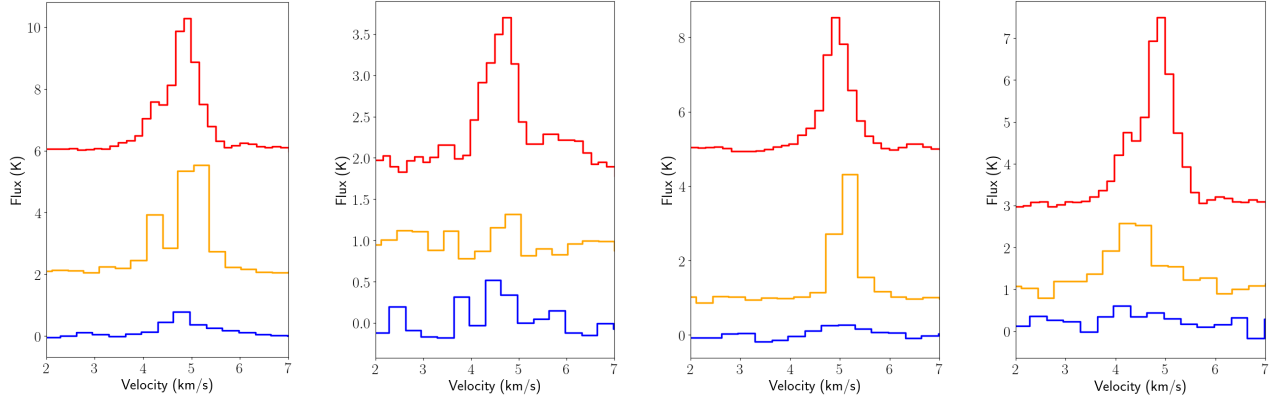


Figure 13. H_2CO spectra toward each sub-region (*left to right*): Main, N, S, and W. Red (top) corresponds to $3(0,3)-2(2,1)$ (218222 MHz), Yellow (middle) corresponds to $3(1,2)-2(1,1)$ (225698 MHz), Blue (bottom) corresponds to $3(0,3)-2(2,1)$ (218475 MHz).

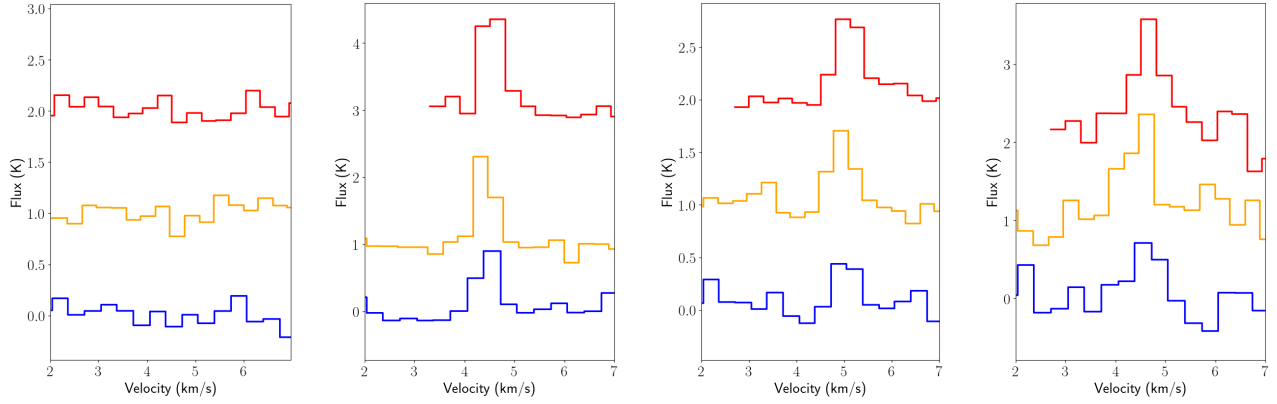


Figure 14. CH_3OH spectra toward each sub-region (*left to right*): Main, N, S, and W. Red (top) corresponds to $5(0,5)-4(0,4)++$ (241791 MHz), Yellow (middle) corresponds to $5(-1,5)-4(-1,4)$ (241767 MHz), Blue (bottom) corresponds to $5(3,2)-4(3,1)$ (218440 MHz). CH_3OH emission is clearly not detected toward the main source.

B. ADDITIONAL INTEGRATED INTENSITY MAPS

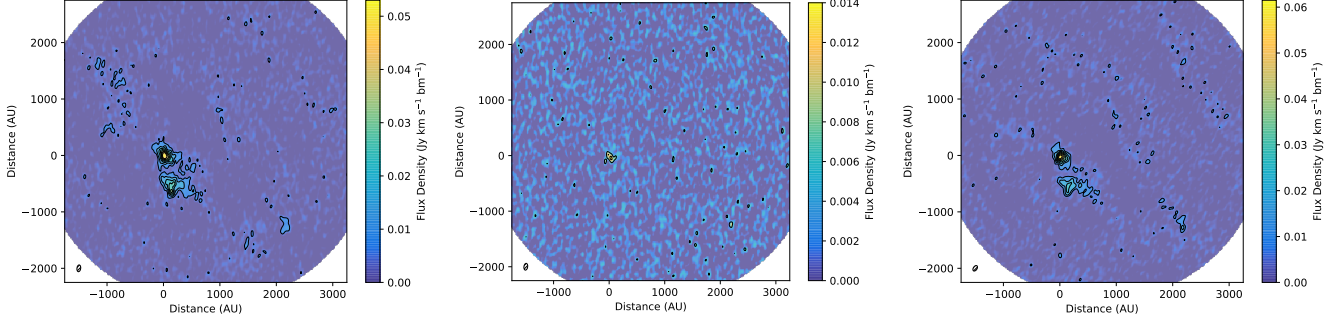


Figure 15. Primary beam corrected integrated intensity maps for H_2CO transitions at (left) 218.222 GHz (between 3.1 and 5.5 km s^{-1}), (middle) 218.475 GHz (between 3.3 and 5.9 km s^{-1}), and (right) 225 GHz (between 3.7 and 6.0 km s^{-1}). The continuum peak is at 0,0 au. (left) Contours start at 3σ (6 mJy/beam km s^{-1}) continue in intervals of 3σ to a peak of 53 mJy/beam km s^{-1} . The beam size is $0.80'' \times 0.43''$. (middle) Contours start at 3σ (6 mJy/beam km s^{-1}) continue in intervals of 3σ to a peak of 14 mJy/beam km s^{-1} . The beam size is $0.81'' \times 0.45''$. (right) Contours start at 3σ (7.5 mJy/beam km s^{-1}) continue in intervals of 3σ to a peak of 61 mJy/beam km s^{-1} . The beam size is $0.72'' \times 0.44''$.

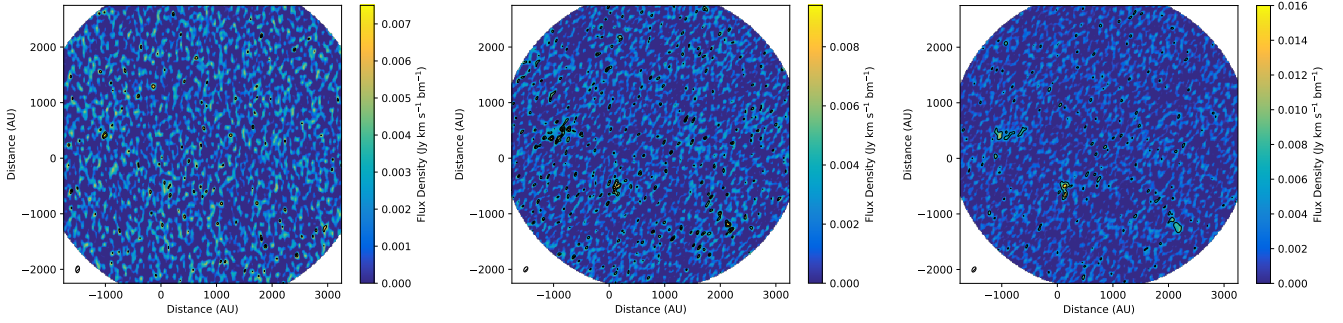


Figure 16. Primary beam corrected integrated intensity maps for CH_3OH transitions at (left) 218.440 GHz (between 4.0 and 5.7 km s^{-1}), (middle) 241.767 GHz (between 3.9 and 6.0 km s^{-1}), and (right) 241.791 GHz (between 3.6 and 5.4 km s^{-1}). The continuum peak is at 0,0 au. (left) Contours start at 3σ (5.4 mJy/beam) continue in intervals of 1σ to a peak of 7 mJy/beam. The beam size is $0.81'' \times 0.45''$. (middle) Contours start at 3σ (4.5 mJy/beam) continue in intervals of 1σ to a peak of 9 mJy/beam. The beam size is $0.68'' \times 0.40''$. (right) Contours start at 3σ (6.0 mJy/beam) continue in intervals of 3σ to a peak of 16 mJy/beam. The beam size is $0.68'' \times 0.40''$.

REFERENCES

- Bally, J., Walawender, J., Luhman, K. L., & Fazio, G. 2006, *AJ*, 132, 1923
- Belloche, A., Parise, B., van der Tak, F. F. S., et al. 2006, *A&A*, 454, L51
- Belloche, A., Schuller, F., Parise, B., et al. 2011, *A&A*, 527, A145
- Bjerkeli, P., Liseau, R., Nisini, B., et al. 2013, *A&A*, 552, L8
- Bolatto, A. D., Wolfire, M., & Leroy, A. K. 2013, *ARA&A*, 51, 207
- Busch, L. A., Belloche, A., Cabrit, S., et al. 2020, *A&A*, 633, A126
- Chen, X., Arce, H. G., Zhang, Q., et al. 2010, *ApJ*, 715, 1344
- Chen, X., Arce, H. G., Dunham, M. M., et al. 2012, *ApJ*, 751, 89
- Cordiner, M. A., Charnley, S. B., Wiström, E. S., et al. 2012, *ApJ*, 744, 131
- Dunham, M. M., Chen, X., Arce, H. G., et al. 2011, *ApJ*, 742, 1
- Dunham, M. M., Crapsi, A., Evans, Neal J., I., et al. 2008, *ApJS*, 179, 249
- Dutta, S., Lee, C.-F., Hirano, N., et al. 2022, *ApJ*, 931, 130. doi:10.3847/1538-4357/ac67a1
- Dzib, S. A., Loinard, L., Ortiz-León, G. N., et al. 2018, *ApJ*, 867, 151
- Friesen, R. K., Pon, A., Bourke, T. L., et al. 2018, *ApJ*, 869, 158. doi:10.3847/1538-4357/aaeff5
- Fujishiro, K., Tokuda, K., Tachihara, K., et al. 2020, *ApJL*, 899, L10
- Furuya, R. S., Kitamura, Y., & Shinnaga, H. 2019, *ApJ*, 871, 137. doi:10.3847/1538-4357/aaf85c
- Goldsmith, P. F. & Langer, W. D. 1999, *ApJ*, 517, 209
- Goldsmith, P. F. 2001, *ApJ*, 557, 736

- Hiramatsu, M., Hayakawa, T., Tatematsu, K., et al. 2007, *ApJ*, 664, 964
- Hirano, N. & Liu, F.-c. 2014, *ApJ*, 789, 50
- Hirano, N. 2019, ALMA2019: Science Results and Cross-Facility Synergies, 90. doi:10.5281/zenodo.3585378
- Knude, J., & Hog, E. 1998, *A&A*, 338, 897
- Koumpia, E., van der Tak, F. F. S., Kwon, W., et al. 2016, *A&A*, 595, A51. doi:10.1051/0004-6361/201528042
- Ladd, E. F., Wong, T., Bourke, T. L., & Thompson, K. L. 2011, *ApJ*, 743, 108
- Larson, R. B. 1969, *MNRAS*, 145, 271
- Lee, J.-E. 2007, in American Astronomical Society Meeting Abstracts, Vol. 211, 89.13
- López-Sepulcre, A., Codella, C., Cesaroni, R., Marcelino, N., & Walmsley, C. M. 2009, *A&A*, 499, 811
- López-Sepulcre, A., Cesaroni, R., & Walmsley, C. M. 2010, *A&A*, 517, A66
- Machida, M. N., Inutsuka, S.-i., & Matsumoto, T. 2008, *ApJ*, 676, 1088
- Marcelino, N., Gerin, M., Cernicharo, J., et al. 2018, *A&A*, 620, A80. doi:10.1051/0004-6361/201731955
- Masunaga, H. & Inutsuka, S.-i. 2000, *ApJ*, 531, 350
- Matsumoto, T., Machida, M. N., & Inutsuka, S.-i. 2017, *ApJ*, 839, 69. doi:10.3847/1538-4357/aa6a1c
- Maureira, M. J., Arce, H. G., Dunham, M. M., et al. 2020, *MNRAS*. doi:10.1093/mnras/staa2894
- Noble, J. A., Theule, P., Mispelaer, F., et al. 2012, *A&A*, 543, A5
- Okoda, Y., Oya, Y., Sakai, N., et al. 2020, *ApJ*, 900, 40. doi:10.3847/1538-4357/aba51e
- Omukai, K. 2007, *PASJ*, 59, 589
- Penteado, E. M., Walsh, C., & Cuppen, H. M. 2017, *ApJ*, 844, 71
- Pineda, J. E., Arce, H. G., Schnee, S., et al. 2011, *ApJ*, 743, 201
- Price, D. J., Tricco, T. S., & Bate, M. R. 2012, *MNRAS*, 423, L45
- Reipurth, B., Nyman, L. A., & Chini, R. 1996, *A&A*, 314, 258
- Saigo, K. & Tomisaka, K. 2011, *ApJ*, 728, 78
- Sánchez-Monge, Á., López-Sepulcre, A., Cesaroni, R., et al. 2013, *A&A*, 557, A94
- Spear, S., Maureira, M. J., Arce, H. G., et al. 2021, *ApJ*, 923, 231. doi:10.3847/1538-4357/ac3083
- Tielens, A. G. G. M. & Hagen, W. 1982, *A&A*, 114, 245
- Tsitali, A. E., Belloche, A., Commerçon, B., et al. 2013, *A&A*, 557, A98
- Tomida, K., Tomisaka, K., Matsumoto, T., et al. 2010, *ApJ*, 714, L58
- Väisälä, M. S., Harju, J., Mantere, M. J., et al. 2014, *A&A*, 564, A99
- van der Tak, F. F. S., van Dishoeck, E. F., & Caselli, P. 2000, *A&A*, 361, 327
- Vastel, C., Bottinelli, S., Caux, E., et al. 2015, SF2A-2015: Proceedings of the Annual meeting of the French Society of Astronomy and Astrophysics, 313
- Wakelam, V., Coutens, A., Gratier, P., et al. 2022, *A&A*, 666, A191. doi:10.1051/0004-6361/202243459
- Wu, Y., Wei, Y., Zhao, M., et al. 2004, *A&A*, 426, 503
- Young, A. K., Bate, M. R., Harries, T. J., et al. 2019, *MNRAS*, 487, 2853